



Article

MIL-53(Fe)@perylene Diimide All-Organic Heterojunctions for the Enhanced Photocatalytic Removal of Pollutants and Selective Oxidation of Benzyl Alcohol

Kaiyang Shi ¹, Fulin Wang ¹, Xiangwei Li ¹, Weiya Huang ¹, Kang-Qiang Lu ¹ , Changlin Yu ^{2,*} and Kai Yang ^{1,*} 

¹ School of Chemistry and Chemical Engineering, Jiangxi University of Science and Technology, Ganzhou 341000, China

² Key Laboratory of Petrochemical Pollution Process and Control, School of Chemical Engineering, Guangdong University of Petrochemical Technology, Maoming 525000, China

* Correspondence: yuchanglinjx@163.com (C.Y.); yangkai@jxust.edu.cn (K.Y.)

Abstract: Organic semiconductors are promising materials for the photocatalytic treatment of pollutants and organic synthesis. Herein, MIL-53(Fe)@perylene diimide (PDI) organic heterojunctions were constructed by ultrasonic assembly using PDI as the co-catalyst, and PDI organic supramolecular material was uniformly distributed on the surfaces of MIL-53(Fe). The most effective M53@PDI-20 organic heterojunctions achieved 72.7% photodegradation of rhodamine B (10 mg/L) within 50 min and a 99.9% reduction in Cr(VI) (10 mg/L) for 150 min, and the corresponding apparent degradation rate constants were higher than a single component. Meanwhile, the conversion rate of benzyl alcohol over M53@PDI-20 achieved 91.5% for 5 h with a selectivity of above 90% under visible light exposure, which was more than double that of PDI. The well-matched band structures and the strong π - π bonding interactions between MIL-53(Fe) and PDI can increase the electron delocalization effect to facilitate the transfer and separation of photogenerated carriers. Lots of oxidative reactive species (h^+ , $\bullet O_2^-$ and $\bullet OH$) also played a great contribution to the strong oxidation capacity over the heterojunctions system. This work suggests that MIL-53(Fe)@PDI organic heterojunctions may be a promising material for pollutant removal and organic synthesis.

Keywords: MIL-53(Fe); PDI; Rhodamine B degradation; Cr(VI) reduction; selective oxidation of benzyl alcohol



Citation: Shi, K.; Wang, F.; Li, X.; Huang, W.; Lu, K.-Q.; Yu, C.; Yang, K. MIL-53(Fe)@perylene Diimide All-Organic Heterojunctions for the Enhanced Photocatalytic Removal of Pollutants and Selective Oxidation of Benzyl Alcohol. *Catalysts* **2023**, *13*, 471. <https://doi.org/10.3390/catal13030471>

Academic Editor: Shun-cheng Lee

Received: 19 January 2023

Revised: 15 February 2023

Accepted: 20 February 2023

Published: 23 February 2023



Copyright: © 2023 by the authors. Licensee MDPI, Basel, Switzerland. This article is an open access article distributed under the terms and conditions of the Creative Commons Attribution (CC BY) license (<https://creativecommons.org/licenses/by/4.0/>).

1. Introduction

The rapid technological boom of recent decades has led to a significant increase in environmental pollution problems, accompanied by a wide range of pollutants that are difficult to treat [1]. As a renewable source of energy, solar energy is clean and environmentally friendly, making it one of the most promising options for future development. Thus, scientific research on the efficient utilization, fast conversion, and storage of solar energy is an important issue [2–4]. Semiconductor photocatalysis systems have gained attention because of their energy efficiency, low cost, and environmental friendliness. The advances in science and technology have used the reaction process of photocatalysts that develops light energy (sunlight) to transform some chemical reactions under the harsh conditions of operable reactions under relatively mild conditions [5,6]. The photogenerated carriers {electrons (e^-) and holes (h^+)} produced on semiconductors can transform light energy into oxidation and reduction energy. For example, the photocatalytic degradations of toxic, hazardous organic dyes and inorganic heavy metal hazardous chemicals are suitable candidates for the removal of pollutants from water [7–9].

Organic semiconductor materials have emerged as a new area for research in photocatalysis. Organic supramolecular materials such as perylene diimide (PDI) have shown enormous potential by their self-assembly techniques for photocatalytic applications [10,11]. In particular,

typical n-type PDI organic supramolecular semiconductors are gaining attention and being more widely developed in the field of photocatalysis due to their superior optical properties and high stability [12]. Zhu et al. [13] reported the synthesis of supramolecular materials with the introduction of carboxyl groups on the acyl of PDI, giving it higher photocatalytic property and stability, and good charge mobility and electron affinity [14]. As early as 1997, PDI molecules were found to be able to open the rings of certain phenolic organic pollutants by photocatalysis under alkaline conditions [15]. It has also been used in photocatalytic oxygen production [16,17], the degradation of organic pollutants [10,18], and the mineralization of phenols [19]. With their special electronic and photophysical properties, they have also been used for optical and electronic applications with chemical modifications [20,21]. However, PDI still suffers from the defect that the photogenerated carriers are more prone to recombination, resulting in their low photocatalytic performance.

Metal–organic frameworks (MOFs) are appropriate for the construction of heterojunctions' photocatalytic materials with various active substances due to their variable structure, simple synthesis, and high stability, which are commonly used for the degradation of various pollutants and heavy metal ions in the environment [22]. The units are connected by an organic framework linking units to form metal ion nodes, which form porous materials through coordination [23], and MOFs have a wide range of applications in catalysis [24,25]. MIL-53(Fe), as a typical iron-based MOF material, is considered to be a three-dimensional porous iron-based material composed of Fe(III) centers and terephthalic acid, which has a stable, ordered structure, functional ability, porosity, and multiple active sites [26,27]. Meanwhile, MIL-53 (iron) can also absorb visible light from 420 to 800 nm, which is a wider absorption range than other MOF materials [28–30]. In addition, the valence change in the metal center renders the catalytic activity. However, the quickly photogenerated electrons and hole recombination remain an obstacle for MIL-53(Fe) to overcome. Therefore, the construction of heterostructures with other photocatalysts is an efficient approach [31,32].

Stimulated by the above discussion, all-organic heterojunction materials were constructed by introducing PDI organic supramolecular into the MIL-53(Fe) framework structure, which exhibited excellent removals of rhodamine B (RhB) and Cr(VI) in an aqueous solution. These pollutants in wastewater have a deleterious effect on environmental health [32]. MIL-53(Fe)@PDI all-organic heterojunctions also achieve an exceptional photocatalytic performance in the selective oxidation of benzyl alcohol to aldehydes. It is ascribed to the strong interactions of Z-scheme interfacial charge transfer and migration by π – π bonds, providing a possible transfer mechanism for MIL-53(Fe)@PDI heterojunctions.

2. Results and Discussion

2.1. Structural Characterizations

To determine the successful synthesis of MIL-53(Fe)@PDI, the physical phase structure was analyzed using XRD. As displayed in Figure 1a, the characteristic diffraction peaks corresponding to MIL-53(Fe) in the XRD pattern of MIL-53(Fe) appear at around 9.3° , 12.7° and 25.7° , which is in agreement with the crystal structure of MIL-53(Fe) reported in the literature [33,34]. The diffraction peaks of PDI supramolecular material range from 5° to 30° [10], and the characteristic diffraction peaks between 24° and 28° are considered to be characteristic of π – π stacking structures [35,36], which facilitate the transfer of charge carriers. MIL-53(Fe)@PDI heterojunctions show approximately the same XRD patterns as the original MIL-53(Fe). However, the diffraction peaks corresponding to PDI are not evident in the M53@PDI-5 spectra, probably because the PDI content is highly coated on the surfaces of MIL-53(Fe). As the loading of PDI increases, PDI diffraction peaks in the range 24 – 28° can be seen, indicating the successful bonding of MIL-53(Fe) with PDI to form the heterojunctions.

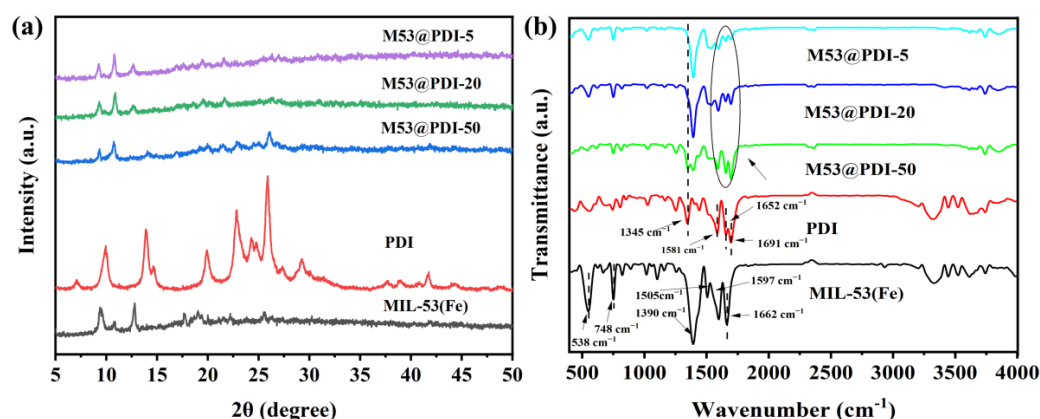


Figure 1. XRD patterns (a) and FT-IR spectra (b) of PDI, MIL-53(Fe) and MIL-53(Fe)@PDI heterojunctions.

To examine the functional groups over MIL-53(Fe)@PDI materials in detail and analyze their surfaces' chemical structures, the IR spectra of the PDI, MIL-53(Fe), and MIL-53(Fe)@PDI samples are shown in Figure 1b. Whilst 1597 cm^{-1} is assigned to the benzene ring backbone stretching vibrational peak of MIL-53(Fe), the two strong absorption peaks at 1505 cm^{-1} and 1390 cm^{-1} correspond to the asymmetric and symmetric vibrational peaks of MIL-53(Fe), respectively, in agreement with the previous report [37]. The absorption peak at 1662 cm^{-1} is due to the stretching of the C=O bond. The peak at 748 cm^{-1} is ascribed to the bending vibration of the C–H bond on the benzene ring (organic linker) [38] and the characteristic absorption peak at 538 cm^{-1} is derived from the Fe–O bond between Fe(III) and terephthalic acid, indicating the formation of Fe-oxo clusters between the inorganic metal and the carboxylate group of the organic linker [33], and the presence of a dicarboxylate linkage in the framework. The absorption peaks of the PDI supramolecule are mainly located at 1691 cm^{-1} (C=O) and 1652 cm^{-1} (C=C), while a series of different ratios of MIL-53(Fe)@PDI can be observed with the characteristic vibrational peaks in the same position as that of both PDI and MIL-53(Fe), which is further evidence of the formation of organic heterojunctions.

X-ray photoelectron spectra were used to determine the elemental compositions of the samples. From the full spectra of MIL-53(Fe) and M53@PDI-20 samples in Figure S2, it can be seen that the elements of C, O, N, and Fe are all present in the M53@PDI-20 heterojunction material and the obvious N element is only present in M53@PDI-20. In Figure 2a, the peaks with binding energies of 284.8 eV and 288.7 eV correspond to C=C on the benzoic acid ring and C=O on terephthalic acid [39]. In addition, the binding energy of 285.8 eV on M53@PDI-20 is attributed to the C–N signal peak. The Fe 2p in Figure 2b shows two peaks at 725.8 and 711.9 eV for Fe 2p_{1/2} and Fe 2p_{3/2}, respectively. The distance between these two peaks is approximately 13.9 eV, and there is also a neutral peak at 717.3 eV, which is unique to MIL-53(Fe) [40], thus further demonstrating the successful synthesis of MIL-53(Fe). In the O 1s spectrum (Figure 2c), two peaks at 531.9 and 530.5 eV are attributed to the oxygen component of the H₂BDC and Fe–O bond on the organic bond of MIL-53(Fe) [3]. Additionally, in the O spectrum of M53@PDI-20, the peaks at 529.4, 530.1, 531.5 and 532.8 eV, where 529.4 and 532.8 eV correspond to C–O bonds in surfaces which adsorbed H₂O and PDI [41], respectively, while 530.1 and 531.5 eV are consistent with Fe–O, C=O in MIL-53(Fe) and the binding energy is shifted towards lower binding energy shift. At the same time, the position of Fe 2p of M53@PDI-20 is shifted by 0.5 eV in the direction of the decreasing binding energy, indicating an increase in the electron cloud density on the Fe element and a strong interaction between MIL-53(Fe) and M53@PDI-20. In addition, there is a clear peak of N 1s on the M53@PDI-20 in Figure 2d, and the element N is specific to PDI, so MIL-53(Fe) and PDI were successfully integrated together to form the heterojunction.

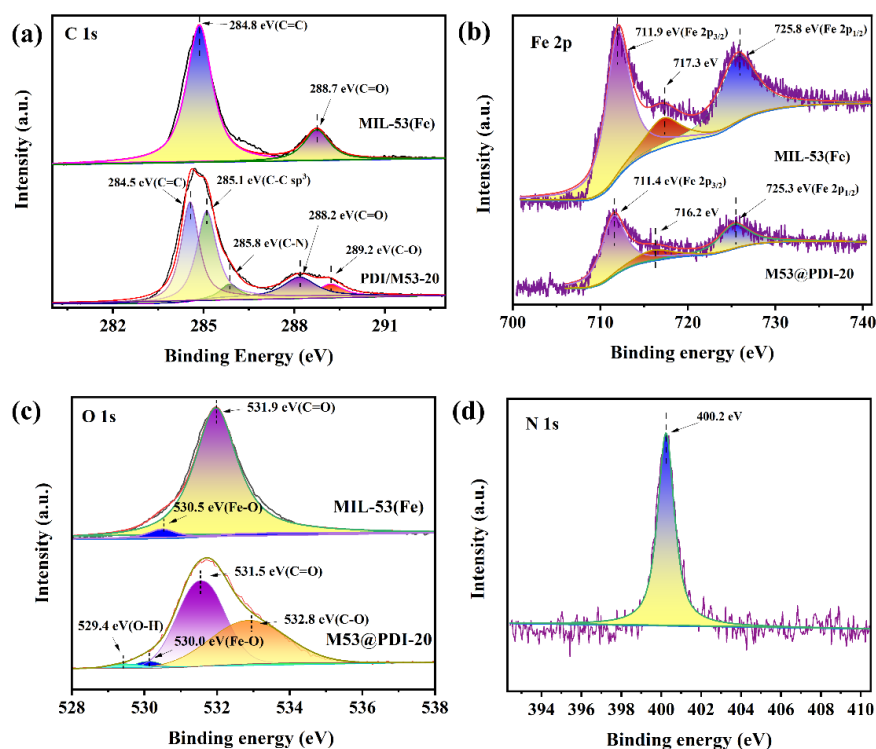


Figure 2. XPS spectra of MIL-53(Fe) and M53@PDI-20: (a) C 1s; (b) Fe 2p; (c) O 1s; (d) N 1s.

2.2. Morphological Analysis

Sample morphologies were investigated with SEM and TEM. The result of Figure 3a reveals that MIL-53(Fe) shows a polyhedral shuttle structure, which is in line with what was previously observed for MIL-53(Fe) [17], while the self-assembled PDI is the small-sized willow-like nanofibers from the TEM of Figure 3b. A clear interface between MIL-53(Fe) and PDI can be observed in the TEM of Figure 3c–d. The PDI supramolecule is grown on the surfaces of the polyhedral MIL-53(Fe) (Figure S3). This is also a direct indication of the successful MIL-53(Fe)@PDI heterojunctions. Figure 3e–h show the elemental distributions on M53@PDI-20, where C, N, O, and Fe are uniformly spread out. It can be speculated that PDI is tightly wrapped around MIL-53(Fe), which greatly enhances both the charge transfer and separation.

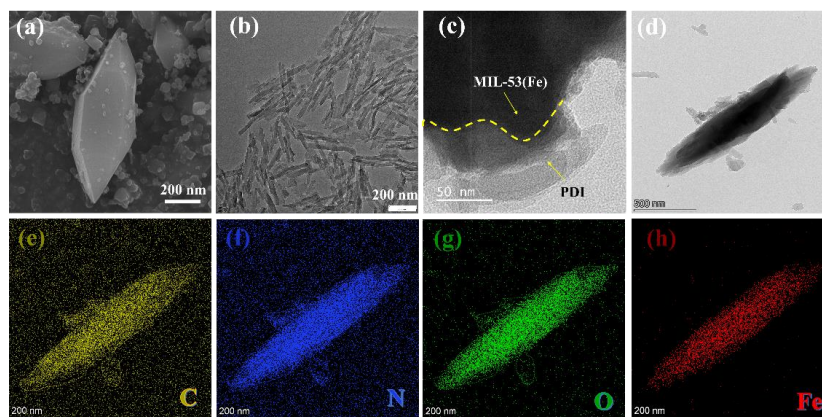


Figure 3. SEM image of (a) MIL-53(Fe), (b) TEM of PDI, and (c,d) M53@PDI-20, (e–h) elemental mapping image of M53@PDI-20 heterojunctions.

2.3. UV–Vis DRS Analysis

As shown in Figure 4a, both PDI and MIL-53(Fe) have strong absorption in the UV–visible region. MIL-53(Fe)@PDI heterojunctions show the wide range of visible light absorption and the absorption values of MIL-53(Fe) increase with the loading of PDI. The absorption edge of PDI is located at approximately 750 nm, which is significantly wider than that of MIL-53(Fe). Due to the interaction between PDI and MIL-53(Fe), the introduction of PDI gives rise to a new absorption at 420–700 nm in the heterojunction, thus enhancing the visible light absorption range. The bandgap energy (E_g) can be estimated using the tangent intercept of the $(\alpha hv)^{1/2}$ pair of photon energy (hv) as the following formula. Figure 4b,c show the $(\alpha hv)^{1/2}$ vs. (hv) figure of the band gap. E_g values for PDI, MIL-53(Fe), M53@PDI-50, M53@PDI-20, and M53@PDI-5 were evaluated to be approximately 1.70 eV, 2.72 eV, 2.15 eV, 2.62 eV, and 2.73 eV. In comparison with MIL-53(Fe), the E_g of MIL-53(Fe)@PDI is reduced, which could generate more carriers under visible light excitation.

$$(\alpha hv)^{1/2} = A(hv - E_g)^n \quad (1)$$

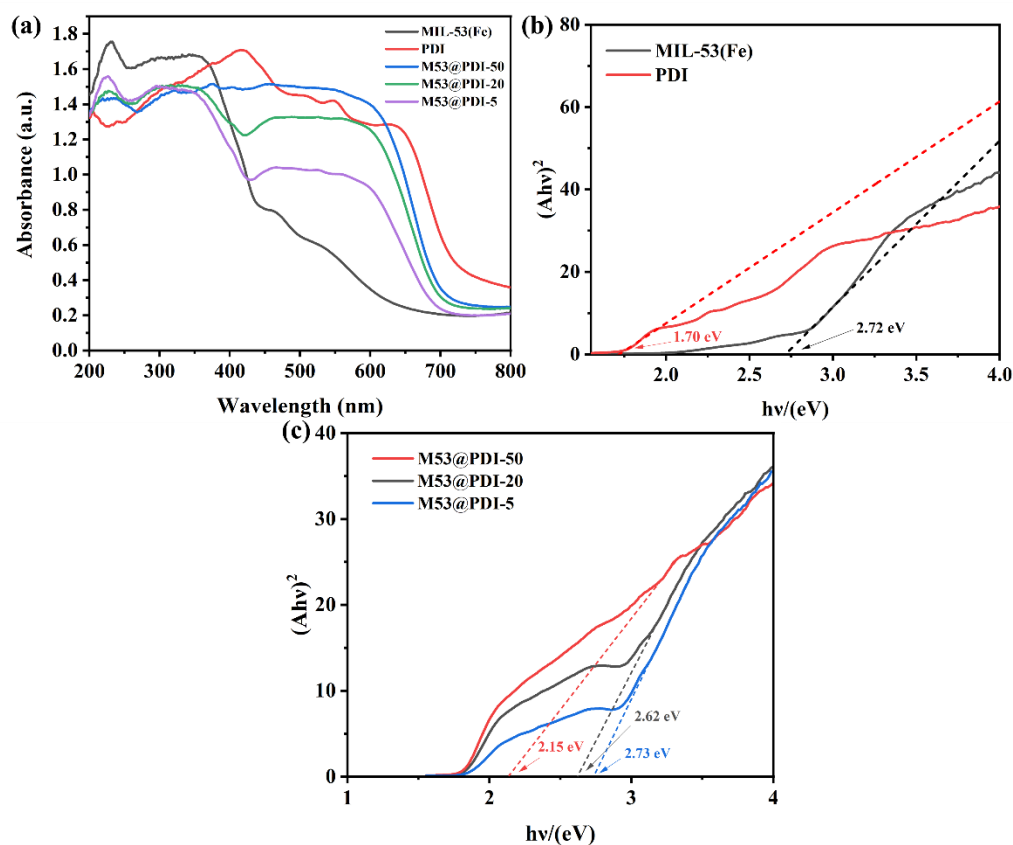


Figure 4. (a) UV–Vis diffuse reflectance spectra; (b) Tauc plots of MIL-53(Fe), PDI, and MIL-53(Fe)@PDI heterojunctions; and (c) Tauc plots of M53@PDI-50,20,5.

2.4. Photocatalytic Performances

2.4.1. Photocatalytic Degradation of RhB and Cr(VI) Pollutants

The photocatalytic performances were evaluated by the RhB degradation and Cr(VI) reduction. As shown in Figure 5a,c,g, MIL-53(Fe)@PDI heterojunctions for degrading 10 mg/L and 20 mg/L RhB exhibited excellent photocatalytic capabilities under 400 W metal halide lamp irradiation and the comparisons of activities were M53@PDI-20 > M53@PDI-5 > M53@PDI-50 > MIL-53(Fe) > PDI. The degradation rate for 10 mg/L RhB over M53@PDI-20 can increase from 42.4% to approximately 72.7% within 50 min of photocatalytic reaction, and while its degradation rate for 20 mg/L RhB increases from 37.5% to approximately 47.1%. As shown in the fitted curves of Figure 5b,d, the pseudo primary kinetic constant for the degradation of

M53@PDI-20 heterojunctions for 10 mg/L RhB is 2.6 and 2.3 times higher than those for PDI and MIL-53(Fe), respectively, and 3.0 and 1.2 times higher than those for PDI and MIL-53(Fe) for 20 mg/L RhB, respectively. These results indicate that the heterojunctions constructed by a small amount of PDI and MIL-53(Fe) could significantly improve the photocatalytic capabilities (Figure 5e). Furthermore, M53@PDI-20 exhibits benign stability for the degradation of 10 mg/L RhB in three consecutive cycles (Figure 5f). Meanwhile, after the photocatalytic reaction of 150 min, M53@PDI-20 heterojunctions significantly improve the reduction in the Cr(VI) solution, achieving 99.9% reduction for 10 mg/L Cr(VI), and its pseudo primary kinetic constant for the reduction of 10 mg/L Cr(VI) is higher than those of PDI and MIL-53(Fe) by a factor of 15.2 and 1.4 (Figure 5h).

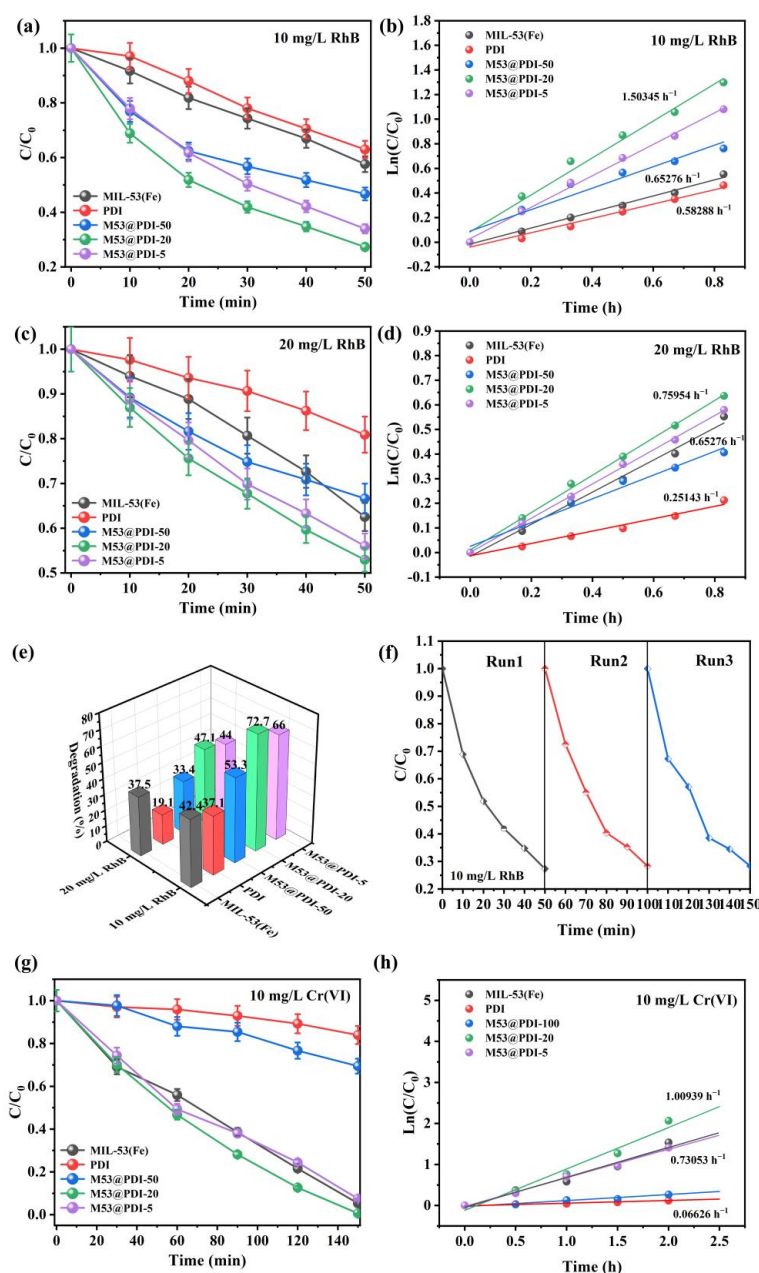


Figure 5. Photocatalytic capabilities for the degradations of (a,b) 10 mg/L, (c,d) 20 mg/L RhB, and the reduction of 10 mg/L Cr(VI) solution, (e) RhB removal rates over all samples, (f) the cycling degradation of 10 mg/L RhB on M53@PDI-20 and (g,h) over PDI, MIL-53(Fe) and MIL-53(Fe)@PDI heterojunctions under 400 W metal halide lamp irradiation, respectively.

2.4.2. Evaluation of the Selective Oxidation of Benzyl Alcohol

Furthermore, according to Figure 6, the photocatalytic effects of MIL-53(Fe) and PDI on the selective oxidation of benzyl alcohol are relatively weak, with conversions of only 44.7% and 40.2%, probably due to its low charge separation efficiencies. After loading the PDI organic supramolecule into MIL-53(Fe), the heterojunctions show a substantial increase in the photocatalytic rate for benzyl alcohol, and the conversion rate of benzyl alcohol over M53@PDI-20 organic heterojunctions increases to 91.5%. Additionally, the selectivities of these samples are all above 90%, also corresponding to the previous analysis, and M53@PDI-20 reaches a maximum selectivity of 99%.

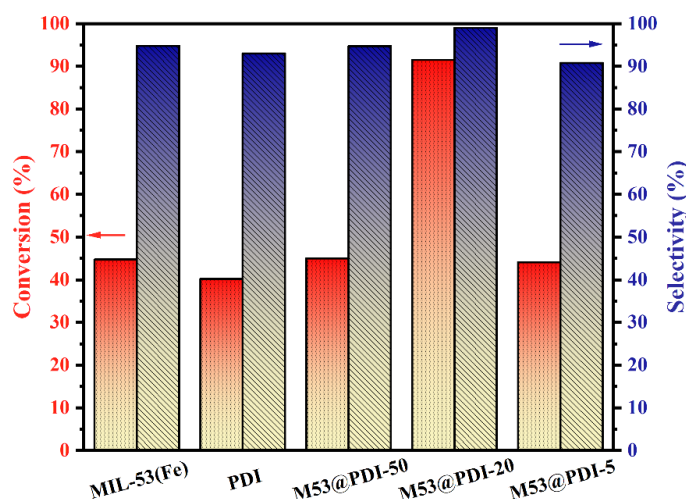


Figure 6. Selective oxidation of benzyl alcohol over PDI, MIL-53(Fe), and MIL-53(Fe)@PDI heterojunctions under visible light irradiation.

2.5. Photoelectrochemical and Optical Properties

The efficiency of interfacial charge separation was further tested through EIS Nyquist plots, as shown in Figure 7a. In comparison with MIL-53(Fe), the arc radii of M53@PDI-5, M53@PDI-20, and M53@PDI-50 heterojunctions are smaller, and the order of the arc radii is from smallest to largest: M53@PDI-20 < M53@PDI-50 < M53@PDI-5 < MIL-53(Fe) < PDI. This indicates that the introduction of PDI is conducive to the charge transfer on the surfaces of the heterojunctions, and the shorter the arc diameter is, the lower the charge transfer resistance is [42]. The photogenerated carriers for photocatalytic reactions can be effectively separated by M53@PDI-20, reducing the charge transfer resistance. Similarly, the transient photocurrent response is an essential technique for studying the behavior of the photogenerated charge transfer and separation. Typically, the higher photocurrent response implies that photogenerated charges can be efficiently separated to achieve excellent photocatalytic activity [43]. The higher π - π stacking and strong π - π interaction can facilitate the formation of electron leaving domains, which facilitating the transport of photoelectrons and improving the separation of photogenerated carriers [44]. According to Figure 7b, the transient photocurrent of M53@PDI-20 is improved and superior to those of M53@PDI-5, M53@PDI-50, PDI, and MIL-53(Fe), which indicates that the construction of heterojunctions enhances the separation of photogenerated electrons and holes. Additionally, this result corresponds to the photocatalytic activity.

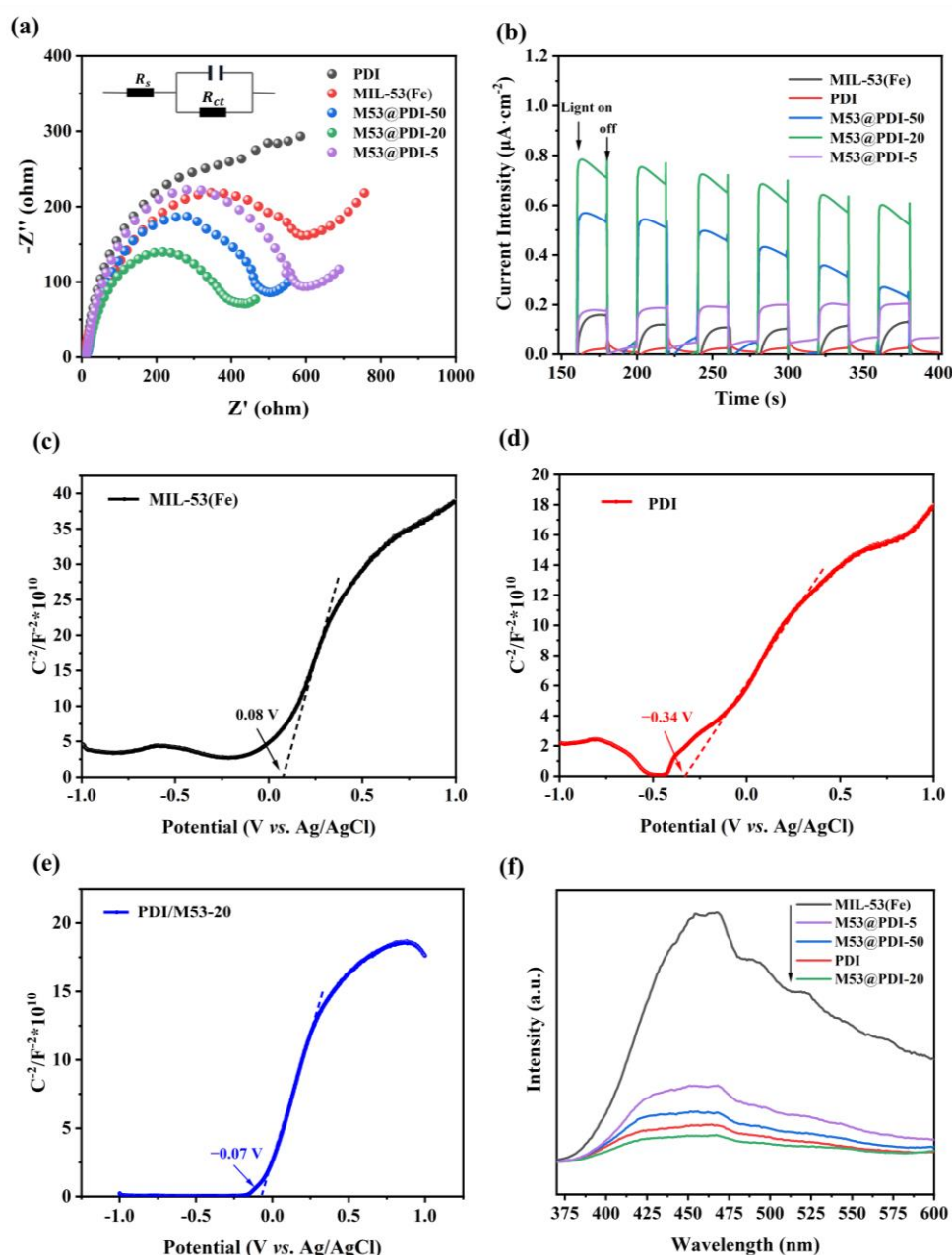


Figure 7. (a) EIS Nyquist plots and (b) transient photocurrent responses of the samples, Mott-Schottky plots of (c) MIL-53(Fe), (d) PDI and (e) M53@PDI-20 and (f) the steady-state photoluminescence (PL) spectra.

In addition, the Mott-Schottky (M-S) test was carried out to further demonstrate the effect of PDI on the energy level structure of MIL-53(Fe). As can be seen from Mott-Schottky of the PDI and MIL-53(Fe) in Figure 7c–e, the slopes by the linear fits of the curves are positive, indicating that PDI and MIL-53(Fe) are all typical n-type semiconductors. The flat-band potentials of MIL-53(Fe), PDI, and M53@PDI-20 in a neutral electrolyte of 0.1 mol/L Na_2SO_4 with respect to a standard hydrogen electrode (NHE) are 0.277 V, -0.143 V, and 0.127 V, respectively, relative to 0.08 eV, -0.34 eV, and -0.07 eV for Ag/AgCl electrodes. The conversion formula of the Ag/AgCl electrode and NHE is $E_{\text{NHE}} = E_{\text{Ag/AgCl}} + 0.197$. An n-type semiconductor has a conduction band that is roughly 0.1–0.2 eV lower than a flat-band semiconductor [30]. Thus, the conduction band positions of MIL-53(Fe) and PDI vs. NHE are -0.077 eV and -0.343 eV, respectively. From the band gaps of MIL-53(Fe) and PDI of UV-Vis DRS (Figure 4a) and the empirical formula ($E_{\text{VB}} = E_{\text{CB}} + E_{\text{g}}$) [45], the valence bands of MIL-53(Fe) and PDI are calculated to be 2.643 V and 1.357 V, respec-

tively. To further confirm the accuracy of the band structure, we also consider directly using the VB-XPS method. The VB-XPS diagram was used to obtain the valence band potential (E_{VB-XPS}). The corresponding EVB and XPS of MIL-53 (Fe) and PDI were measured to be 2.86 and 1.55 eV, respectively (Figure S7a,b). Then, the EVB responding to the standard hydrogen electrode (E_{VB}) can be calculated according to the following formula: $E_{VB} = \varphi + E_{VB-XPS} - 4.44$ [46], where φ is the work function of the instrument (4.2 eV). Therefore, the E_{VB} of MIL-53 (Fe) and PDI are calculated to be 2.62 and 1.31 eV, which is basically the same as that estimated by the Mott–Schottky equation.

Photoluminescence spectra can be used to analyze the carrier transfer over the heterojunctions, where the ineffective charge separation provides the greatest recombination, which can be converted into thermal energy or fluorescence emission during the process. The higher intensity of its emission peak signifies the lower separation efficiency of the photogenerated electrons/holes [47]. Figure 7f shows the MIL-53(Fe) > M53@PDI-100 > M53@PDI-5 > M53@PDI-20 intensity sequential fluorescence spectra. The formation of M53@PDI-20 heterostructures between PDI and MIL-53(Fe) exhibits the lowest electron and hole complexation rates, which realizes excellent charge transfer properties in agreement with the results of the photocatalytic activities.

2.6. Contact Angle Analysis

In general, the higher surface energies and smaller contact angles reflect a greater hydrophilic capability. From Figure 8a–d, it can be observed that M53@PDI-20 exhibits a smaller contact angle compared with MIL-53(Fe) under different contaminant droplets, and while the surface energies of M53@PDI-20 are 59.76 mN/m on 10 mg/L of RhB solution (Figure 8b) and 43.47 mN/m on 10 mg/L of Cr(IV) solution (Figure 8d), respectively, these are higher than the solid surface energies of the MIL-53(Fe) sample (18.75 mN/m (Figure 8a) for 10 mg/L of RhB and 22.31 mN/m (Figure 8c) for 10 mg/L of Cr(IV)). This indicates that the modification of PDI makes MIL-53(Fe) prompt the adsorption and activation of pro-contaminant solutions, where M53@PDI-20 could adsorb more contaminants to facilitate its elimination.

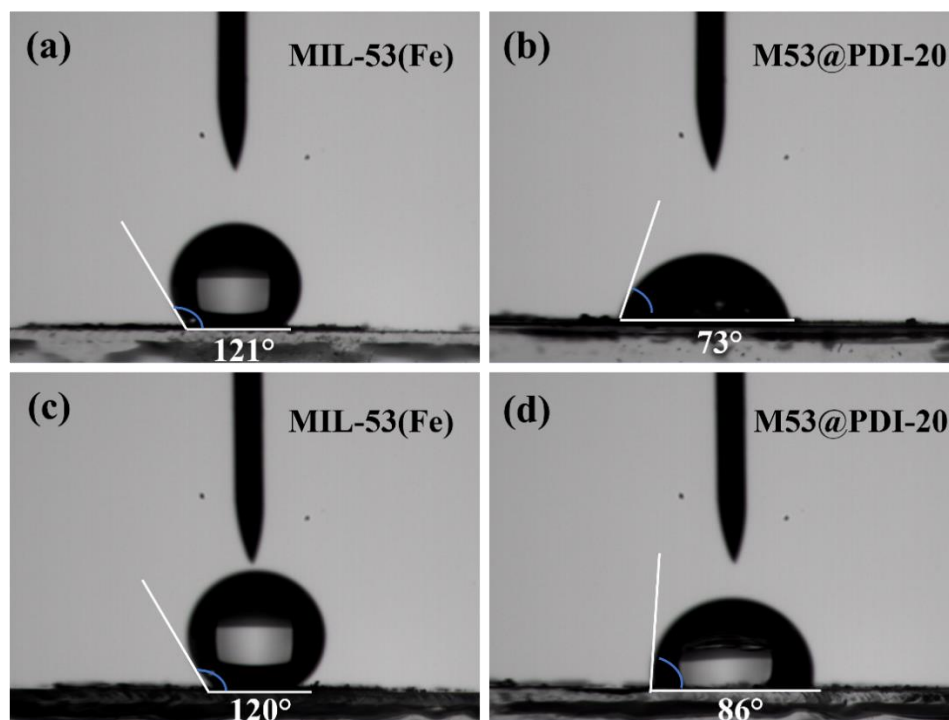


Figure 8. Images of contact angles of MIL-53(Fe) (a) and M53@PDI-20 (b) with 10 mg/L RhB solution; images of contact angles of MIL-53(Fe) (c) and M53@PDI-20 (d) with 10 mg/L Cr(IV) solution.

2.7. Active Species Capturing Experiments and Possible Mechanism

To explore the major reactive species in this degradation reaction of the RhB solution over M53@PDI-20, 1 mmol/L of trapping agent was added into the 10 mg/L RhB substrate prior to the dark reaction to capture the major reactive species. Of these, tert-butanol was used to capture hydroxyl radicals ($\cdot\text{OH}$), p-benzoquinone (p-BZQ) captured the superoxide radicals ($\bullet\text{O}_2^-$), and EDTA-2Na captured the photogenerated holes (h^+) [48]. As from Figure 9, it can be seen that the degradation of RhB over M53@PDI-20 significantly decreases from 72.7% to 42.3% with the addition of EDTA-2Na. The result indicates that h^+ has the highest degradation effect on RhB pollutants, followed by $\cdot\text{OH}$ and $\bullet\text{O}_2^-$.

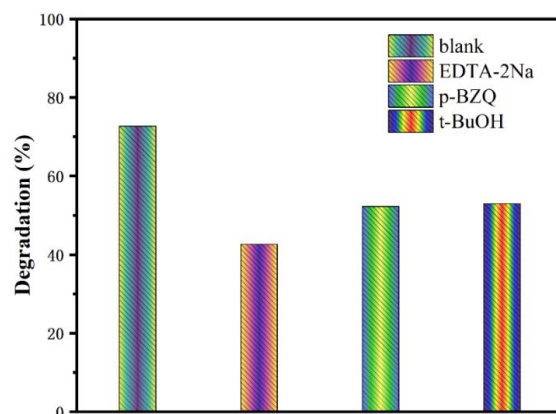


Figure 9. Active species capturing experiments for the degradation of 10 mg/L RhB over M53@PDI-20.

According to the above analysis, an electron transfer mechanism based on the Z-scheme is proposed as shown in Figure 10 and Table S1. MIL-53(Fe) and PDI can be simultaneously photoexcited under visible light irradiation. Due to the suitable band alignment and close contact between MIL-53(Fe) and PDI, the electrons in the conduction band of MIL-53(Fe) could migrate to PDI to recombine with holes on its valence band. Therefore, the electron aggregation on the PDI conduction band with substantial reducing property can reduce Cr(VI) and reduce O_2 to $\bullet\text{O}_2^-$, while the holes on the valence band of MIL-53(Fe) could oxidize RhB and benzyl alcohol (1.88 eV vs. NHE). The stability is also improved by the effective charge separation and transfer of Z-scheme heterojunctions.

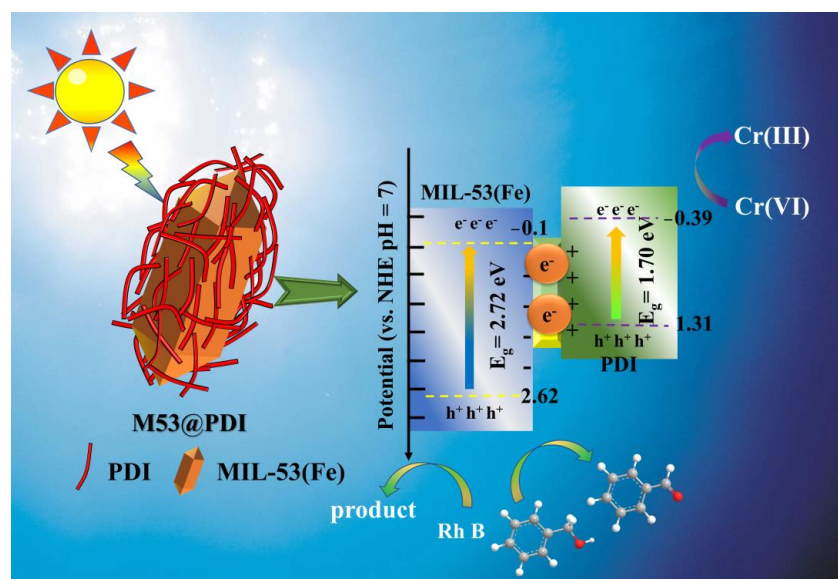


Figure 10. A possible photocatalytic mechanism over MIL-53(Fe)@PDI heterojunctions.

3. Experimental Section

All chemicals were of analytical grade and used without further purification.

3.1. Synthesis of MIL-53(Fe)

A quantity of $\text{FeCl}_3 \cdot 6\text{H}_2\text{O}$ and terephthalic acid (H_2BDC) was weighed into a 100 mL beaker and a quantity of *N,N*-dimethylformamide (DMF) was added. The molar ratio was 1:1:280. The solution was stirred for 1 h until the solid was fully dissolved into a clarified solution, after which it was transferred to a 100 mL reactor liner containing polytetrafluoroethylene and hydrothermally reacted at 150 °C for 24 h. After the reaction was completed, the product was washed by centrifugation with DMF and anhydrous ethanol several times to obtain a pale yellow powder, which was then activated at 100 °C for 10 h in a blast oven [31].

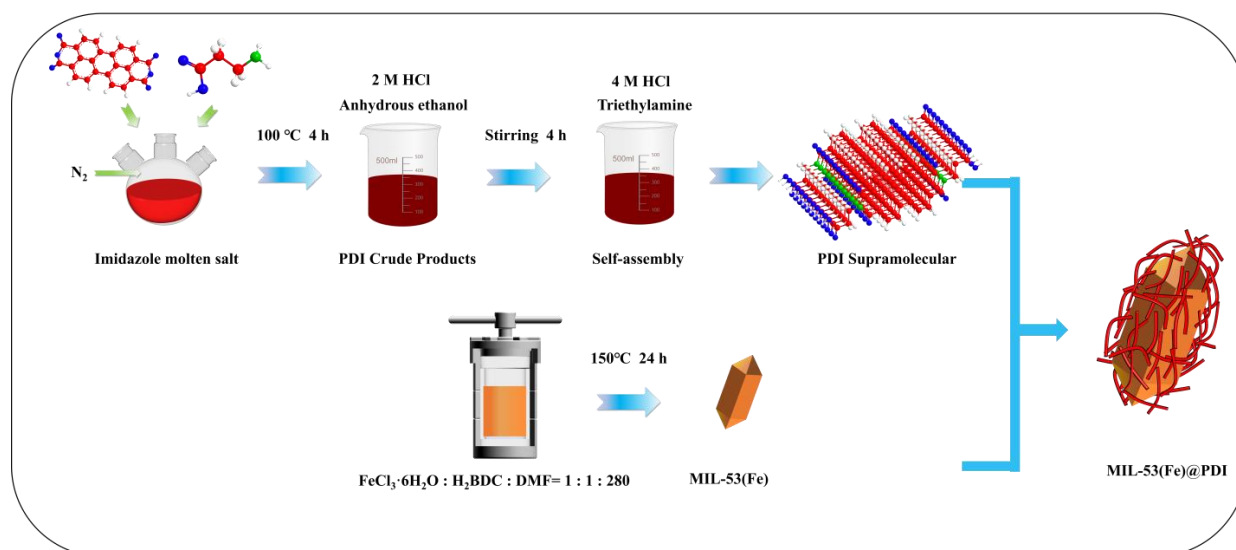
3.2. Synthesis of PDI

A combination of 3.50 mmol of 3,4,9,10-tetracarboxylic acid dianhydride, 28 mmol of β -amino acid, and 18 g of imidazole was mixed into an oil bath at 100 °C and stirred under nitrogen for 4 h. The product was then left to cool to 25 °C. A total of 100 mL of anhydrous ethanol and 300 mL of 2.0 M hydrochloric acid (HCl) were added and stirred for 12 h. The suspension was filtered through an aqueous membrane (0.45 μm) and repeatedly washed with deionized water until the supernatant was neutral. The product was dried at 60 °C for 24 h to give the crude PDI product [14].

Subsequently, 0.54 g of the dried PDI crude product was placed in 200 mL of deionized water. The organic base triethylamine TEA (800 μL) was added under stirring and stirred for 1 h. Then, 35 mL hydrochloric acid (4.0 M) was added and stirred for 3 h. Dark-red solid PDI nanofibers were formed and dried under vacuum at 70 °C for 12 h after extraction to obtain the PDI supramolecular material.

3.3. Synthesis of PDI/MIL-53(Fe) All-Organic Heterojunctions

A certain amount of MIL-53(Fe) and PDI was weighed together and placed in a polytetrafluoroethylene liner, and the corresponding amount of anhydrous ethanol was added to ultrasonically disperse the product for 30 min. The samples were labeled as M53@PDI-5, M53@PDI-20, and M53@PDI-50 according to the mass percentage of PDI material (5%, 20%, and 50%). A schematic illustration of the synthesis procedure for MIL-53(Fe)@PDI is shown in Scheme 1.



Scheme 1. Schematic representation of the process of the synthesized MIL-53(Fe)@PDI.

3.4. Photocatalytic Performances

3.4.1. Photocatalytic Degradations of the Simulated Pollutants

The photocatalytic activity of 10 (or 20) mg/L RhB was tested using a metal halide lamp (400 W). Its optical power is 83.1 mW. The photochemical reactor was cooled with circulating condensate to ensure that the experiments were carried out at 25 °C. Disperse 25 mg of the sample into 50 mL of 10 or 20 mg/L RhB solution and add to a quartz tube. The solution was darkly reacted for 40 min before illumination to achieve equilibrium between physisorption and desorption, after which a 400 W metal halide lamp was switched on and 3–5 mL of suspension was picked up in a centrifuge tube every 10 min. The suspension was centrifuged at high speed and the supernatant was taken for the absorbance testing of RhB. Using the following equation, we calculated the degradation rate D_1 based on the concentration change,

$$D_1 = (1 - C_0/C) \times 100\% = (1 - A_0/A) \times 100\% \quad (2)$$

where C_0 and C are the initial concentrations of the pollutant and the concentration at the moment after degradation, respectively, and A_0 and A represent the absorbance of the pollutant at the starting moment and moment t after degradation, respectively.

3.4.2. Photocatalytic Cr(VI) Reduction

The photocatalytic reduction of the Cr(VI) solution was carried out using a 400 W metal halide lamp as the simulated light source. Disperse 25 mg of the sample into 50 mL of 10 mg/L Cr(VI) solution and add to a quartz tube. At the end of the dark reaction for 40 min, the metal halide lamp was switched on and 3–5 mL of suspension was taken in a centrifuge tube at 30 min intervals. The suspensions were separated in a high-speed centrifuge. The absorbance of Cr(VI) was spectrophotometrically determined by diphenylcarbonyldihydrazide: 1 mL of supernatant was taken with a pipette into a 10 mL volumetric flask, which was then fixed with dilute sulphury acid (0.2 mol/L) to the graduated line of the flask and finally 300 L of GB 7467-87 color developer was added dropwise for the chromogenic reaction. It was shaken well and held for 3–5 min until the color development is complete. The absorbance of Cr(VI) can be measured by a UV spectrophotometer at a wavelength of approximately $\lambda = 554$ nm, where the Cr(VI) reduction rate can be calculated.

3.4.3. Photocatalytic Selective Oxidation of Benzyl Alcohol

The selective catalytic oxidation of benzyl alcohol was carried out in the visible light of a 500 W xenon lamp (500 W xenon lamp $\lambda > 420$ nm). Twenty milligrams of catalyst was added to a quartz reactor with 10 μ L of benzyl alcohol and 2 mL of trifluoro toluene. Oxygen was introduced for 15 min while the reactor was fed with circulating condensate to ensure that the experiment was carried out at 25 °C To bring the benzyl alcohol substrate into full contact with the catalyst, the reaction was mixed under dark conditions for 30 min. Reaction occurred under light conditions for 4 h. The suspension was filtered to remove the catalyst and the supernatant was taken for analysis. The calibration of the benzyl alcohol oxidation baseline was 2 μ L, 4 μ L, 6 μ L, 8 μ L or 10 μ L of benzyl alcohol or benzaldehyde and 2 mL of trifluoro toluene was added into the reactor, whilst other conditions remained unchanged (no light for 30 min and lighting for 4 h). The standard curves were made by gas chromatography analysis (Agilent Technologies GC 7820A, Santa Clara, CA, USA) (Figure S1).

3.5. Characterization

The main characterization tools in this work are as follows. X-ray powder diffraction (XRD, Bruker, Billerica, MA, USA) was acquired by Model Bruker D8 Advance polycrystalline (powder) diffractometer with X-ray tube (Cu target, $K\alpha$ rays = 0.15418 nm) and a scanning speed 10°/min. Fourier transform infrared spectra (FT-IR) were measured with a Nicolet-470 infrared Fourier spectrometer. X-ray photoelectron spectra (XPS) could be

acquired from the Thermo Scientific™ K-Alpha™ X-ray photoelectron spectrometer. The scanning electron microscope (SEM, FEI, Hillsboro, OR, USA) was from Model MLA650F from FEI, USA. Transmission electron microscopy (TEM, FEI, Hillsboro, OR, USA) was carried out using a Talos F200S. Ultraviolet–visible diffuse reflectance spectra (UV–Vis DRS, SHIMADZU UV-2600, Kyoto, Japan) were obtained with a Shimadzu Japan UV-2600 UV–Vis spectrophotometer and the fluorescence spectra (PL) were analyzed with an FLS980 fluorescence spectrometer at an excitation wavelength of $\lambda = 280$ nm. The photoelectrochemical properties of the samples such as photoinduced current (IT), electrochemical impedance (EIS, CHENHUA, Shanghai, China), and Mott–Schottky (M-S) were performed using the CHI660E electrochemical workstation. For the tests, the working electrode was that some sample was pre-coated onto an indium tin oxide glass sheet, Ag/AgCl was as the reference electrode and the Pt plate was as the auxiliary electrode. The electrolyte for IT and M-S tests was 0.1 mol/L Na₂SO₄, and the electrolyte for EIS was 0.1 mol/L K₃Fe(CN)₆ and K₄Fe(CN)₆ buffer solution.

4. Conclusions

As a result, MIL-53(Fe)@PDI heterojunctions with high redox capacities from MIL-53(Fe) and PDI supramolecular materials were synthesized by ultrasonic assembly method. The optimized M53@PDI-20 indicated the improvement in the degrading Rh B, in which the rate constant of 10 mg/L Rh B removal was 2.6 and 2.3 times higher than that of PDI and MIL-53(Fe), respectively. The rate constant in the degrading 20 mg/L was 3.0 and 1.2 times higher than that of PDI and MIL-53(Fe) RhB, respectively. The reactive species (h^+ , $\bullet O_2^-$ and $\bullet OH$) generated in the photocatalytic process could greatly improve the oxidation ability. For the Cr(VI) reduction (10 mg/L) and selective oxidation of benzyl alcohol, M53@PDI-20 exhibited the complete Cr(VI) reduction and efficient benzyl alcohol selective oxidation. This suggests that the addition of PDI organic supramolecules greatly improved the redox effect of MIL-53(Fe), which was attributed to all-organic heterojunctions to enhance the solar light utilization and effectively promote the charge separation and transfer via π – π interaction. This provides a new idea for improving the photocatalytic performance of MOF materials.

Supplementary Materials: The following supporting information can be downloaded at: <https://www.mdpi.com/article/10.3390/catal13030471/s1>, Figure S1. Standard curves for (a) benzyl alcohol and (b) benzaldehyde; Figure S2. Full spectra of MIL-53(Fe) and M53@PDI-20 samples; Figure S3. SEM image of M53@PDI-20; Figure S4. Active species capture experiments for the reduction of 10 mg/L Cr(VI) on M53@PDI-20; Figure S5. (a) Metal halide lamp (400 W), (b) the measured optical power of metal halide lamp (400 W); and (c) photocatalytic reaction device; Figure S6. (a) Synergistic degradation diagram of M53@PDI-20 samples; (b) degradation rates of single and mixed degradates; and (c) color development reactions of singly and synergistically degraded Cr(VI); Figure S7. VB-XPS spectra of (a) MIL-53(Fe); and (b) PDI; and Table S1. Band energy levels of MIL-53(Fe) and PDI.

Author Contributions: Conceptualization, K.Y.; methodology, K.Y., C.Y. and K.-Q.L.; investigation, K.S.; resources, K.Y., C.Y., K.-Q.L. and W.H.; data curation, X.L.; writing—original draft preparation, K.S. and F.W.; writing—review and editing, K.S. and X.L.; visualization, K.S.; supervision, K.Y. and C.Y.; project administration, K.Y. and C.Y.; funding acquisition, K.Y. and C.Y. All authors have read and agreed to the published version of the manuscript.

Funding: We are grateful for financial support from National Natural Science Foundation of China (21962006, 22272034), Jiangxi Provincial Academic and Technical Leaders Training Program—Young Talents (20204BCJL23037), Program of Qingjiang Excellent Young Talents, JXUST (JXUSTQJB2020005), Ganzhou Young Talents Program of Jiangxi Province (204301000111), Postdoctoral Research Projects of Jiangxi Province in 2020 (204302600031), Jiangxi Province “Double Thousand Plan” (Yang Kai, Hou Yang), Guangdong Province Universities and Colleges Pearl River Scholar Funded Scheme (2019), and Jiangxi Provincial Natural Science Foundation (20224BAB203018, 20212BAB213016).

Data Availability Statement: Not applicable.

Conflicts of Interest: The authors declare no conflict of interest.

References

1. Murdoch, M.; Waterhouse, G.I.; Nadeem, M.A.; Metson, J.B.; Keane, M.A.; Howe, R.F.; Llorca, J.; Idriss, H. The Effect of Gold Loading and Particle Size on Photocatalytic Hydrogen Production from Ethanol over Au/TiO₂ Nanoparticles. *Nat. Chem.* **2011**, *3*, 489–492. [[CrossRef](#)] [[PubMed](#)]
2. Murgolo, S.; Franz, S.; Arab, H.; Bestetti, M.; Falletta, E.; Mascolo, G. Degradation of Emerging Organic Pollutants in Wastewater Effluents by Electrochemical Photocatalysis on Nanostructured TiO₂ Meshes. *Water Res.* **2019**, *164*, 114920. [[CrossRef](#)] [[PubMed](#)]
3. Yang, Z.; Xu, X.; Liang, X.; Lei, C.; Wei, Y.; He, P.; Lv, B.; Ma, H.; Lei, Z. MIL-53(Fe)-Graphene Nanocomposites: Efficient Visible-Light Photocatalysts for the Selective Oxidation of Alcohols. *Appl. Catal. B Environ.* **2016**, *198*, 112–123. [[CrossRef](#)]
4. Tayebi, M.; Masoumi, Z.; Kolaei, M.; Tayyebi, A.; Tayebi, M.; Seo, B.; Lim, C.-S.; Kim, H.-G.; Lee, B.-K. Highly Efficient and Stable WO₃/MoS₂-MoO_x Photoanode for Photoelectrochemical Hydrogen Production; a Collaborative Approach of Facet Engineering and P-N Junction. *Chem. Eng. J.* **2022**, *446*, 136830. [[CrossRef](#)]
5. Chen, F.; Huang, H.; Guo, L.; Zhang, Y.; Ma, T. The Role of Polarization in Photocatalysis. *Angew. Chem. Int. Ed.* **2019**, *58*, 10061–10073. [[CrossRef](#)]
6. Masoumi, Z.; Tayebi, M.; Kolaei, M.; Lee, B.-K. Improvement of Surface Light Absorption of ZnO Photoanode Using a Double Heterojunction with α -Fe₂O₃/g-C₃N₄ Composite to Enhance Photoelectrochemical Water Splitting. *Appl. Surf. Sci.* **2023**, *608*, 154915. [[CrossRef](#)]
7. Wang, Y.; Liu, M.; Wu, C.; Gao, J.; Li, M.; Xing, Z.; Li, Z.; Zhou, W. Hollow Nanoboxes Cu_{2-x}S@ZnIn₂S₄ Core-Shell S-Scheme Heterojunction with Broad-Spectrum Response and Enhanced Photothermal-Photocatalytic Performance. *Small* **2022**, *18*, e2202544. [[CrossRef](#)]
8. Xiao, M.; Zhang, L.; Luo, B.; Lyu, M.; Wang, Z.; Huang, H.; Wang, S.; Du, A.; Wang, L. Molten-Salt-Mediated Synthesis of an Atomic Nickel Co-Catalyst on TiO₂ for Improved Photocatalytic H₂ Evolution. *Angew. Chem. Int. Ed.* **2020**, *59*, 7230–7234. [[CrossRef](#)]
9. Peng, X.; Wu, J.; Zhao, Z.; Wang, X.; Dai, H.; Wei, Y.; Xu, G.; Hu, F. Activation of Peroxymonosulfate by Single Atom Co-N-C Catalysts for High-Efficient Removal of Chloroquine Phosphate via Non-Radical Pathways: Electron-Transfer Mechanism. *Chem. Eng. J.* **2022**, *429*, 132245. [[CrossRef](#)]
10. Dai, W.; Jiang, L.; Wang, J.; Pu, Y.; Zhu, Y.; Wang, Y.; Xiao, B. Efficient and Stable Photocatalytic Degradation of Tetracycline Wastewater by 3D Polyaniline/Perylene Diimide Organic Heterojunction under Visible Light Irradiation. *Chem. Eng. J.* **2020**, *397*, 125476. [[CrossRef](#)]
11. Zhang, L.; Zhao, Y.; Wu, Y.; Jiang, Y.; Wang, Q.; Lin, X.; Song, G.; Huang, K.; Yao, Z. An Efficient Approach for Rapid Detection of Polymyxins B Based on the Optically Active Supramolecular Aggregates of Water-Soluble Perylene Diimide. *Sens. Actuators B Chem.* **2020**, *321*, 128594. [[CrossRef](#)]
12. Li, Y.; Zhang, X.; Liu, D. Recent Developments of Perylene Diimide (PDI) Supramolecular Photocatalysts: A Review. *J. Photochem. Photobiol. C Photochem. Rev.* **2021**, *48*, 100436. [[CrossRef](#)]
13. Liu, D.; Wang, J.; Bai, X.; Zong, R.; Zhu, Y. Self-Assembled PDINH Supramolecular System for Photocatalysis under Visible Light. *Adv. Mater.* **2016**, *28*, 7284–7290. [[CrossRef](#)] [[PubMed](#)]
14. Wang, J.; Shi, W.; Liu, D.; Zhang, Z.; Zhu, Y.; Wang, D. Supramolecular Organic Nanofibers with Highly Efficient and Stable Visible Light Photooxidation Performance. *Appl. Catal. B Environ.* **2017**, *202*, 289–297. [[CrossRef](#)]
15. Gerdes, R.; Woehrl, D.; Spiller, W.; Schneider, G.; Schnurpfeil, G.; Schulz-Ekloff, G. Photo-Oxidation of Phenol and Monochlorophenols in Oxygen-Saturated Aqueous Solutions by Different Photosensitizers. *J. Photochem. Photobiol. A* **1997**, *111*, 65–74. [[CrossRef](#)]
16. Sheng, Y.; Li, W.; Xu, L.; Zhu, Y. High Photocatalytic Oxygen Evolution via Strong Built-In Electric Field Induced by High Crystallinity of Perylene Imide Supramolecule. *Adv. Mater.* **2022**, *34*, e2102354. [[CrossRef](#)] [[PubMed](#)]
17. Wei, Y.; Ma, M.; Li, W.; Yang, J.; Miao, H.; Zhang, Z.; Zhu, Y. Enhanced Photocatalytic Activity of PTCDI-C₆₀ via π - π Interaction. *Appl. Catal. B Environ.* **2018**, *238*, 302–308. [[CrossRef](#)]
18. Zeng, W.; Cai, T.; Liu, Y.; Wang, L.; Dong, W.; Chen, H.; Xia, X. An Artificial Organic-Inorganic Z-Scheme Photocatalyst WO₃@Cu@PDI Supramolecular with Excellent Visible Light Absorption and Photocatalytic Activity. *Chem. Eng. J.* **2020**, *381*, 122691. [[CrossRef](#)]
19. Miao, H.; Yang, J.; Wei, Y.; Li, W.; Zhu, Y. Visible-Light Photocatalysis of PDI Nanowires Enhanced by Plasmonic Effect of the Gold Nanoparticles. *Appl. Catal. B Environ.* **2018**, *239*, 61–67. [[CrossRef](#)]
20. Yin, H.; Sui, M.-Y.; Pan, Q.-Q.; Sun, G.-Y.; Geng, Y. A Series of Bowl-Shaped PDI Dimers Designed for Organic Photovoltaic Cells through Engineering N-Annulated Bridge towards Potential Alternatives of PDI Bridged Dimer Acceptors. *Dye. Pigment.* **2018**, *148*, 394–404. [[CrossRef](#)]
21. Yang, J.; Jing, J.; Li, W.; Zhu, Y. Electron Donor-Acceptor Interface of TPPS/PDI Boosting Charge Transfer for Efficient Photocatalytic Hydrogen Evolution. *Adv. Sci.* **2022**, *9*, e2201134. [[CrossRef](#)] [[PubMed](#)]
22. Bavykina, A.; Kolobov, N.; Khan, I.S.; Bau, J.A.; Ramirez, A.; Gascon, J. Metal-Organic Frameworks in Heterogeneous Catalysis: Recent Progress, New Trends, and Future Perspectives. *Chem. Rev.* **2020**, *120*, 8468–8535. [[CrossRef](#)] [[PubMed](#)]
23. Chakraborty, G.; Park, I.H.; Medishetty, R.; Vittal, J.J. Two-Dimensional Metal-Organic Framework Materials: Synthesis, Structures, Properties and Applications. *Chem. Rev.* **2021**, *121*, 3751–3891. [[CrossRef](#)] [[PubMed](#)]
24. Dhaka, S.; Kumar, R.; Deep, A.; Kurade, M.B.; Ji, S.-W.; Jeon, B.-H. Metal-Organic Frameworks (MOFs) for the Removal of Emerging Contaminants from Aquatic Environments. *Coord. Chem. Rev.* **2019**, *380*, 330–352. [[CrossRef](#)]
25. Lin, Y.; Zhang, Y.; Li, G. Promotion of Sulfameter Degradation by Coupling Persulfate and Photocatalytic Advanced Oxidation Processes with Fe-Doped MOFs. *Sep. Purif. Technol.* **2022**, *282*, 119632. [[CrossRef](#)]

26. George, P.; Chowdhury, P. Enhanced Photocatalytic Performance of Novel S^{2-} Doped MIL-53(Fe) under Visible Light. *J. Alloys Compd.* **2021**, *850*, 156578. [[CrossRef](#)]
27. Dinh Du, P.; Ngoc Hoai, P.; Țălu, Ș. Synthesis of MIL-53(Fe) Metal-Organic Framework Material and Its Application as a Catalyst for Fenton-Type Oxidation of Organic Pollutants. *Adv. Mater. Sci. Eng.* **2021**, *2021*, 5540344. [[CrossRef](#)]
28. Feng, X.; Jena, H.S.; Krishnaraj, C.; Leus, K.; Wang, G.; Chen, H.; Jia, C.; Van Der Voort, P. Generating Catalytic Sites in UiO-66 through Defect Engineering. *ACS Appl. Mater. Interfaces* **2021**, *13*, 60715–60735. [[CrossRef](#)]
29. Fu, Y. Enhanced Photocatalytic CO_2 Reduction over Co-Doped NH_2 -MIL-125(Ti) under Visible Light. *RSC Adv.* **2017**, *7*, 42819–42825. [[CrossRef](#)]
30. Liu, H.; Zhang, J.; Ao, D. Construction of Heterostructured $ZnIn_2S_4@NH_2$ -MIL-125(Ti) Nanocomposites for Visible-Light-Driven H_2 Production. *Appl. Catal. B Environ.* **2018**, *221*, 433–442. [[CrossRef](#)]
31. Liu, X.; Zhou, Y.; Zhang, J.; Tang, L.; Luo, L.; Zeng, G. Iron Containing Metal-Organic Frameworks: Structure, Synthesis, and Applications in Environmental Remediation. *ACS Appl. Mater. Interfaces* **2017**, *9*, 20255–20275. [[CrossRef](#)] [[PubMed](#)]
32. He, Z.; Liang, R.; Zhou, C.; Yan, G.; Wu, L. Carbon Quantum Dots (CQDs)/Noble Metal Co-Decorated MIL-53(Fe) as Difunctional Photocatalysts for the Simultaneous Removal of Cr(VI) and Dyes. *Sep. Purif. Technol.* **2021**, *255*, 117725. [[CrossRef](#)]
33. Huang, W.; Liu, N.; Zhang, X.; Wu, M.; Tang, L. Metal Organic Framework $G-C_3N_4$ /MIL-53(Fe) Heterojunctions with Enhanced Photocatalytic Activity for Cr(VI) Reduction under Visible Light. *Appl. Surf. Sci.* **2017**, *425*, 107–116. [[CrossRef](#)]
34. Du, J.-J.; Yuan, Y.-P.; Sun, J.-X.; Peng, F.-M.; Jiang, X.; Qiu, L.-G.; Xie, A.-J.; Shen, Y.-H.; Zhu, J.-F. New Photocatalysts Based on MIL-53 Metal-Organic Frameworks for the Decolorization of Methylene Blue Dye. *J. Hazard. Mater.* **2011**, *190*, 945–951. [[CrossRef](#)]
35. Chen, H.; Zeng, W.; Liu, Y.; Dong, W.; Cai, T.; Tang, L.; Li, J.; Li, W. Unique MIL-53(Fe)/PDI Supermolecule Composites: Z-Scheme Heterojunction and Covalent Bonds for Upgrading Photocatalytic Performance. *ACS Appl. Mater. Interfaces* **2021**, *13*, 16364–16373. [[CrossRef](#)]
36. Yang, J.; Miao, H.; Jing, J.; Zhu, Y.; Choi, W. Photocatalytic Activity Enhancement of PDI Supermolecular via π - π Action and Energy Level Adjusting with Graphene Quantum Dots. *Appl. Catal. B Environ.* **2021**, *281*, 119547. [[CrossRef](#)]
37. Ma, Y.; Li, M.; Jiang, J.; Li, T.; Wang, X.; Song, Y.; Dong, S. In-Situ Prepared MIL-53(Fe)/BiOI Photocatalyst for Efficient Degradation of Tetracycline under Visible-Light Driven Photo-Fenton System: Investigation of Performance and Mechanism. *J. Alloys Compd.* **2021**, *870*, 159524. [[CrossRef](#)]
38. Cui, Y.; Nengzi, L.; Gou, J.; Huang, Y.; Li, B.; Cheng, X. Fabrication of Dual Z-Scheme MIL-53(Fe)/ α - Bi_2O_3 /g- C_3N_4 Ternary Composite with Enhanced Visible Light Photocatalytic Performance. *Sep. Purif. Technol.* **2020**, *232*, 115959. [[CrossRef](#)]
39. Tang, L.; Lv, Z.; Xue, Y.; Xu, L.; Qiu, W.; Zheng, C.; Chen, W.; Wu, M. MIL-53(Fe) Incorporated in the Lamellar BiOBr: Promoting the Visible-Light Catalytic Capability on the Degradation of Rhodamine B and Carbamazepine. *Chem. Eng. J.* **2019**, *374*, 975–982. [[CrossRef](#)]
40. Geng, N.; Chen, W.; Xu, H.; Ding, M.; Lin, T.; Wu, Q.; Zhang, L. Insights into the Novel Application of Fe-MOFs in Ultrasound-Assisted Heterogeneous Fenton System: Efficiency, Kinetics and Mechanism. *Ultrason. Sonochem.* **2021**, *72*, 105411. [[CrossRef](#)]
41. Wang, X.; Meng, J.; Yang, X.; Hu, A.; Yang, Y.; Guo, Y. Fabrication of a Perylene Tetracarboxylic Diimide–Graphitic Carbon Nitride Heterojunction Photocatalyst for Efficient Degradation of Aqueous Organic Pollutants. *ACS Appl. Mater. Interfaces* **2019**, *11*, 588–602. [[CrossRef](#)] [[PubMed](#)]
42. Zhang, K.; Guan, J.; Mu, P.; Yang, K.; Xie, Y.; Li, X.; Zou, L.; Huang, W.; Yu, C.; Dai, W. Visible and Near-Infrared Driven Yb^{3+}/Tm^{3+} Co-Doped $InVO_4$ Nanosheets for Highly Efficient Photocatalytic Applications. *Dalton Trans.* **2020**, *49*, 14030–14045. [[CrossRef](#)] [[PubMed](#)]
43. Yang, J.; Miao, H.; Li, W.; Li, H.; Zhu, Y. Designed Synthesis of a P- Ag_2S/n -PDI Self-Assembled Supramolecular Heterojunction for Enhanced Full-Spectrum Photocatalytic Activity. *J. Mater. Chem. A* **2019**, *7*, 6482–6490. [[CrossRef](#)]
44. Wang, J.; Liu, D.; Zhu, Y.; Zhou, S.; Guan, S. Supramolecular Packing Dominant Photocatalytic Oxidation and Anticancer Performance of PDI. *Appl. Catal. B Environ.* **2018**, *231*, 251–261. [[CrossRef](#)]
45. Masoumi, Z.; Tayebi, M.; Kolaei, M.; Lee, B.-K. Efficient and Stable Core-Shell α - $Fe_2O_3/WS_2/WO_x$ Photoanode for Oxygen Evolution Reaction to Enhance Photoelectrochemical Water Splitting. *Appl. Catal. B Environ.* **2022**, *313*, 121447. [[CrossRef](#)]
46. Li, X.; Kang, B.; Dong, F.; Zhang, Z.; Luo, X.; Han, L.; Huang, J.; Feng, Z.; Chen, Z.; Xu, J.; et al. Enhanced Photocatalytic Degradation and H_2/H_2O_2 Production Performance of S-PCN/ $WO_{2.72}$ S-Scheme Heterojunction with Appropriate Surface Oxygen Vacancies. *Nano Energy* **2021**, *81*, 105671. [[CrossRef](#)]
47. Yu, Z.; Yang, K.; Yu, C.; Lu, K.; Huang, W.; Xu, L.; Zou, L.; Wang, S.; Chen, Z.; Hu, J.; et al. Steering Unit Cell Dipole and Internal Electric Field by Highly Dispersed Er Atoms Embedded into NiO for Efficient CO_2 Photoreduction. *Adv. Funct. Mater.* **2022**, *32*, 2111999. [[CrossRef](#)]
48. Li, H.; Wang, C.; Bai, X.; Wang, X.; Sun, B.; Li, D.; Zhao, L.; Zong, R.; Hao, D. In-Plane Polarization Induced by the Hydrogen Bonding and π - π Stacking of Functionalized PDI Supramolecules for the Efficient Photocatalytic Degradation of Organic Pollutants. *Mater. Chem. Front.* **2020**, *4*, 2673–2687. [[CrossRef](#)]

Disclaimer/Publisher's Note: The statements, opinions and data contained in all publications are solely those of the individual author(s) and contributor(s) and not of MDPI and/or the editor(s). MDPI and/or the editor(s) disclaim responsibility for any injury to people or property resulting from any ideas, methods, instructions or products referred to in the content.